To simplify the calculation, several assumptions were made. First, the force required for the bent-beam actuator to move itself was assumed to be negligible and neglected from the free-body diagram. Second, the coefficient of static friction, μ_s , for polysilicon deposited by LPCVD, is assumed to be 0.11, as reported by Sundararajan et al [23]. This value for μ_s comes from the seven contact dimples (radius = 3 μ m) on the interrupter plate, which results in a total contact area of 198 μ m². For MEMS contact surfaces, μ_s is dependent on the contact area, as determined by Lumbantobing et al. This paper reports that for contact areas of 25 μ m² and a 100 μ m², the values for μ_s are 0.58 and 0.29, respectively [25]. Clearly, this shows a decreasing trend for increasing contact area, and therefore the value of 0.11 is reasonable. Finally, since the coefficient of kinetic friction, μ_k , is typically less that μ_s , its effect is assumed to be negligible [24]. However, this assumption is based on macro-scale material properties, and the research performed by Lumbantobing et al, suggests this may not be true for micro-scale devices.

Finally, the volume of each component is determined from the designed area of the structures and the layer thicknesses provided in Appendix B for run #68. Using the density of polysilicon to be 2.33 g/cm³ [7], the force required to move all the elements attached to a single actuator is calculated using Equations (4.9) and (4.10). The results are shown in Table 4-3. Since the actuator with the Poly1 interrupter plates have a much longer linkage, which is designed to be 3.5-µm thick (Poly1 + Poly2), the required force is over double that required for the actuator with the Poly2 interrupter plates. However, since both of these forces are much less than the micro-newton force usually produced by electrothermal actuators, it is anticipated that the actuators should be able to move the interrupter components with ease.

Table 4-3. Force required to move a single interrupter element consisting of the plate, linkage, and latch component.

Actuator Element Plate Material	Required Actuator Force (nN)
Poly1	0.0965
Poly2	0.0474

4.5.3 Additional Considerations

The interrupter mechanism described in this thesis was designed as a proof of concept, and as such, it has some limitations that must be considered. For example, the interrupter mechanism does not have its own power supply, and therefore, it requires an external power supply for operation, which is a common requirement for munition fuze components. For instance, many munition items currently have on-board power supplies that derive their power from both electrochemical and electromechanical devices [26]. Additionally, this interrupter mechanism was not specifically designed to sense an environmental condition as a prerequisite to arming (i.e., opening the aperture), which is a fuze requirement under MIL-STD-1316E [27]. Therefore, a valid launch condition must be determined by some other means, before actuation of the interrupter mechanism is enabled.

Potential Power Sources

An example of an electrochemical power source is a thermal battery. Thermal batteries use electrically-initiated pyrotechnic chemicals to melt an initially solid electrolyte material. Other electrochemical power sources use the spin forces generated during launch to distribute an electrolyte into battery cells. These types of

electrochemical batteries are capable of providing a potential difference of approximately 30 V for a minimum discharge time of 30 minutes. An output voltage of this magnitude would be capable of operating the interrupter mechanism described in this research [26].

Two examples of electromechanical power sources are wind-driven generators and pulse-driven generators. Wind-driven generators develop their power as a result of ram air pressure and are capable of producing power outputs of 1-2 W at munition velocities greater than 200 ft/sec. The advantages of using a wind-driven power source are its low cost, essentially limitless shelf life, and simple operation that tends to increase reliability. On the other hand, one type of pulse-driven generator is a piezoelectric transducer that produces a sudden potential difference when the piezoelectric material is mechanically stressed. These devices are capable of instantaneously providing very large voltage outputs as a result of some type of environmental stimuli, such as launch acceleration or weapon impact [26].

Potential Environmental Sensing Capability

This interrupter mechanism, as currently designed, can only function through the operation of four bent-beam electrothermal actuators. As previously discussed, these electrothermal actuators provide linear motion due to the current density in the pre-bent arms causing them to thermally expand. As an alternative approach, it may be possible to induce thermal expansion of the arms through the use of a different energy source, and still produce the same actuation effect.

A unique environment that could provide this potential energy source for operating the actuators is the aerodynamic heating that results from the ballistic environment. Aerodynamic heating is produced as a result of the atmospheric drag

experienced by a munition as it travels through the air. As the munition approaches supersonic speeds, it can absorb a significant amount of heat from the compression of air flowing around the munition body. While the increased temperature tends to vary along the munition body, the maximum temperature increase is at the nose, where the air flow velocity is theoretically zero. Furthermore, the recovery temperature (defined as the temperature that can be recovered at the surface of the fuze, from the maximum temperature at the nose), can be related to the Mach number, M, of the air flow and the ambient temperature, T_a , by the following relationship [26]:

$$T_r = T_a \cdot (1 + 0.2 \cdot r_f \cdot M^2)$$
 (K) (4.11)

where

$$T_r = recovery\ temperature$$
 (K)
 $r_f = correction\ factor$ (dimensionless)

The correction factor accounts for the fact that the temperature at the fuze surface is reduced from the nose temperature. This correction factor is typically approximated to be 0.9, which accounts for a wide range of conditions [26]. If the bent-beam electrothermal actuators presented in this thesis could be linked, via a thermal conduction path, from the nose of the munition to the expanding arms, it may be possible to operate the S&A interrupter device using aerodynamic heating as the energy source. In addition, if this is possible, aerodynamic heating could potentially be used as one of the environmental stimuli that prevents unintentional arming required by MIL-STD-1316E.

Figure 4-24 shows a graphical representation of Equation (4.11), along with some recovery temperature comparisons between typical munition systems as a function of their Mach number. The Mach numbers for these systems come from Table 2-1 and the

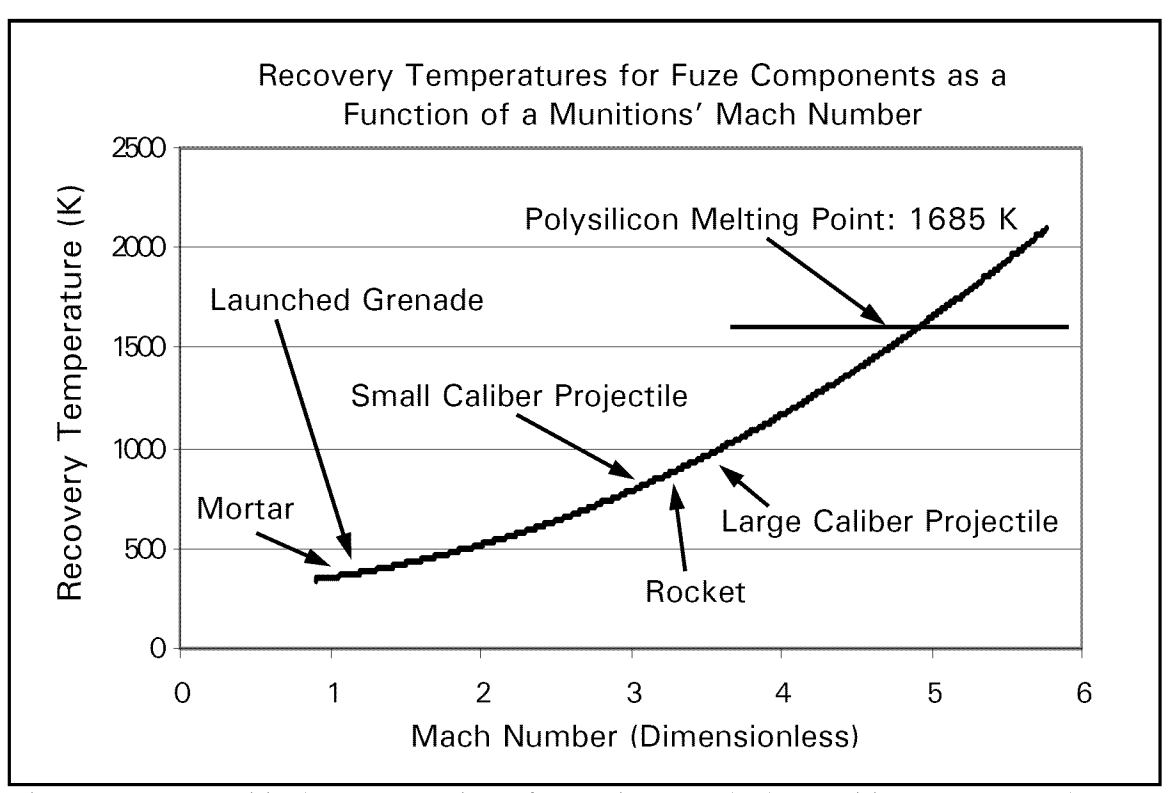


Figure 4-24. Graphical representation of Equation (4.11) along with some comparisons between typical munition systems using the Mach numbers as provided by Table 2-1. Note: all aerodynamic heating temperature for these munition systems are below the melting point of polysilicon.

ambient temperature, T_a , is assumed to be 300 K. As can be seen from the figure, all the recovery temperatures are below 1685 K, which implies the actuators would not suffer from thermal failure due to melting of the polysilicon arms. Furthermore, the small/large caliber projectiles and the rockets are just below the optimal operating temperature (1173 - 1273 K) of the bent-beam actuators as discussed in Section 4.4.1 [18]. Lastly, it should be noted that even though aerodynamic heating is a legitimate environment condition, as of 1994, it had not been used in any known fuze designs to initiate arming. However, it has been used to perform self-destruct functions in some small caliber projectiles [26].

4.6 Summary

This chapter has presented the theory on which the design of the MEMS interrupter mechanism was based. The specific fabrication process used for this research effort was presented along with a discussion of the inherent constraints (e.g., number of releasable layers and layer thicknesses) of this process. This was followed by a detailed discussion of the mechanism designed to interrupt the flyer material in a slapper detonator, as well as the bent-beam electrothermal actuator used to separate the interrupter plates, thereby enabling an unimpeded path for the flyer on it way to initiating the HE pellet. Finally, this chapter concluded with a brief discussion about some theoretical power sources that could be used to power the electrothermal actuators, as well as a potential environmental energy source that could enable a sensing function to be incorporated into this interrupter mechanism. The next chapter will discuss the results of testing that was performed on the actual fabricated devices.

Bibliography

- [1] Koester, David and others. *PolyMUMPs Design Handbook (Revision 11.0)*. MEMSCAP, 2005. August 2005. http://www.memsrus.com/documents/PolyMUMPs.DR.v11.pdf.
- [2] *PolyMUMPs FAQ (Revision 2.0)*. MEMSCAP, 2004. August 2005. http://www.memsrus.com/documents/PolyMUMPs.faq.v2.pdf>.
- [3] Comtois, John H. and Victor M. Bright. "Design techniques for surface-micromachining MEMS processes," *Proceedings of SPIE The International Society for Optical Engineering*. Volume 2639: 211-222 (September 1995).
- [4] Zygo Corporation's NewView 5000[™], Precise, Rapid, Noncontact 3D Surface Profiling. Middlefield: Zygo Corporation, 2001.
- [5] Seely, J. H. and R. C. Chu. *Heat Transfer in Microelectronic Equipment A Practical Guide*. New York: Marcel Dekker, Inc. 1972.
- [6] Kladitis, Paul. Class handout, EENG 636, Microelectromechanical Systems. Graduate School of Engineering and Management, Air Force Institute of Technology, Wright-Patterson AFB OH, January 2005.
- [7] Kovacs, Gregory T. A. *Micromachined Transducers Sourcebook*. Boston: The McGraw Hill Company, 1998.
- [8] Sinclair, Michael J. "A High Force Low Area MEMS Thermal Actuator," *The Seventh Intersociety Conference on Thermal and Thermomechanical Phenomena in Electronic Systems.* Volume 1, 127-132. IEEE Press, 2000.
- [9] Comtois, John Henry. Structures and Techniques for Implementing and Packaging Complex, Large Scale Microelectromechanical Systems Using Foundry Fabrication Processes. Air Force Institute of Technology (AU), Wright-Patterson AFB OH, May 1996 (ADA310747).
- [10] Reid, James R. *Microelectromechanical Isolation of Acoustic Wave Resonators*. Air Force Institute of Technology (AU), Wright-Patterson AFB OH, November 1996 (ADA321364).
- [11] Reid, James R. "Force Measurements of Polysilicon Thermal Micro-Actuators," *Proceedings of the SPIE The International Society for Optical Engineering*. Volume 2882: 296-306 (October 1996).

- [12] Park, J. S., L. L. Chu, E. Siwapornsathain, A. D. Oliver, and Y. B. Gianchandani. "Long Throw and Rotary Output Electro-Thermal Actuators Based on Bent-Beam Suspensions," *Proceedings of the Thirteenth Annual International Conference on Micro Electro Mechanical Systems*. 680 – 685. IEEE Press, 2000.
- [13] Kolesar, Edward S. and others. "In-Plane Tip Deflection and Force Achieved With Asymmetrical Polysilicon Electrothermal Microactuators," *Thin Solid Films*. Volume 377-378, 719-726 (December 2000).
- [14] Comtois, John H., Victor M. Bright, and Mark W. Phipps. "Thermal Microactuators for Surface-Micromachining Processes," *Proceedings of SPIE The International Society for Optical Engineering*. Volume 2642: 10-21 (October 1995).
- [15] Que, L., J.-S. Park, and Y. B. Gianchandani. "Bent-Beam Electro-Thermal Actuators for High Force Applications," *Proceedings of the IEEE Micro Electro Mechanical Systems (MEMS)*. 31-36. IEEE Press, 1999.
- [16] Comtois, John H., M. Adrian Michalicek, and Carole Craig Barron. "Characterization of Electrothermal Actuators and Arrays Fabricated in a Four-Level, Planarized Surface-Micromachined Polycrystalline Silicon Process." *Proceedings of the 1997 International Conference on Solid-State Sensors and Actuators*. Volume 2, 769 772. IEEE Press, 1997.
- [17] Szabo, Francis R. *Demonstrating Optothermal Actuators for an Autonomous MEMS Microrobot*. MS Thesis, AFIT/GE/ENG/04-23. School of Engineering and Management, Air Force Institute of Technology (AU), Wright-Patterson AFB OH, March 2004 (ADA426469).
- [18] Sinclair, Michael J. and Kerwin Wang. "Thermal Actuator Improvements: Tapering and Folding," *Proceedings of the SPIE The International Society for Optical Engineering*. Volume 5116: 237-251 (April 2003).
- [19] Srikar, V. T. and Stephen D. Senturia. "Thermoelastic Damping in Fine-Grained Polysilicon Flexural Beam Resonators," *Journal of Microelectromechanical Systems*. Volume 11, No. 5, 499-504. IEEE Press, 2002.
- [20] National Aeronautics and Space Administration. *MEMS Reliability Assurance Guidelines for Space Applications*. Ed. Brian Stark. JPL Publication 99-1. Pasadena: Jet Propulsion Laboratory, January 1999.
- [21] Simon, Andrew L. and David A. Ross. *Principles of Statics and Strength of* Materials. Dubuque: Wm. C. Brown Company Publishers, 1983.

- [22] Sharpe Jr., W. N., K. Jackson, G. Coles, and D. A. LaVan. "Young's Modulus and Fracture Strength of Three Polysilicons," *Proceedings of Materials Science of Microelectromechanical Systems (MEMS) Devices III.* Volume 657: 551-556. Materials Research Society, 2001.
- [23] Sundararajan, Sriram and Bharat Bhushana. "Static Friction and Surface Roughness Studies of Surface Micromachined Electrostatic Micromotors Using an Atomic Force Friction/Force Microscope," *Journal of Vacuum Science and Technology*. Volume 19(4), 1777-1785 (July-August 2001).
- [24] Sternheim, Morton M. and Joseph W. Kane. *General Physics* (2nd Edition). New York: John Wiley and Sons, 1991.
- [25] Lumbantobing, Ari and Kyriakos Komvopoulos. "Static Friction in Polysilicon Surface Micromachines," *Journal of Microelectromechanical Systems*. Volume 14, Issue 4, 651-663 (August 2005).
- [26] MIL-HDBK-757(AR). "Fuzes." Military Handbook. 15 April 1994.
- [27] MIL-STD-1316E. "Safety Criteria For Fuze Design." Department of Defense Design Criteria Standard. 10 July 1998.

5. Experimental Procedure and Results

In an effort to determine the overall effectiveness of the conceptual MEMS interrupter mechanism designed for this research effort, several individual aspects of the complete device were examined in an attempt to quantify their performance characteristics. These test results will provide valuable insight into the feasibility of using this device as an interrupter in a solid-state slapper detonator. The devices used in most of these tests were fabricated in PolyMUMPs run #68, with the only exception being some of the process test structures, which were designed in both run #68 and run #69. (Appendix C shows all the design layouts produced as part of this research.)

To begin, the structures used to determine the limits of the PolyMUMPs fabrication process will be examined, along with the impact of those results on the design of the interrupter mechanism. Next, the experiments performed on the stand-alone bent-beam electrothermal actuators will be discussed and some measured performance data will be presented. Finally, the complete interrupter mechanism will be investigated to determine if it is capable of operating as intended. In addition, some measured data from these tests will be presented in order to quantify its performance.

5.1 PolyMUMPs Fabrication Process Test Structures

Since the limits of the fabrication process can vary slightly between each run, several test structures were designed with the goal of determining the minimum tolerances for device width and device spacing. These features are relevant to the design of the interrupter mechanism and knowing these specific limits can help determine if any

design flexibility exists. For example, the minimum line width for both Poly1 and Poly2 is listed by the PolyMUMPs design rules to be 3 µm [1]. If it can be determined that narrower line widths are possible, it may enable more effective actuators to be designed, since it is desirable for the width of the expanding arms, in a bent-beam actuator, to be as small as possible in order to maximize bending near the anchors [2]. Figure 5-1 shows the fabricated width test structures, for both Poly1 and Poly2. It can be readily observed that the 1-µm wide beam is the minimum beam width that could be fabricated in this run. Nevertheless, notice that a larger width would most likely be required for any practical device, since the 1-µm wide beams do not appear to be very structurally sound. In addition, notice that the 0.5-µm wide beam could not be fabricated at all in this fabrication run, as evident by the material left behind in the anchor etch holes. The specific structures in Figure 5-1 are from run #69, and the test structures in run #68 produced similar results, however, this does not guarantee that every fabrication run will produce the same results.

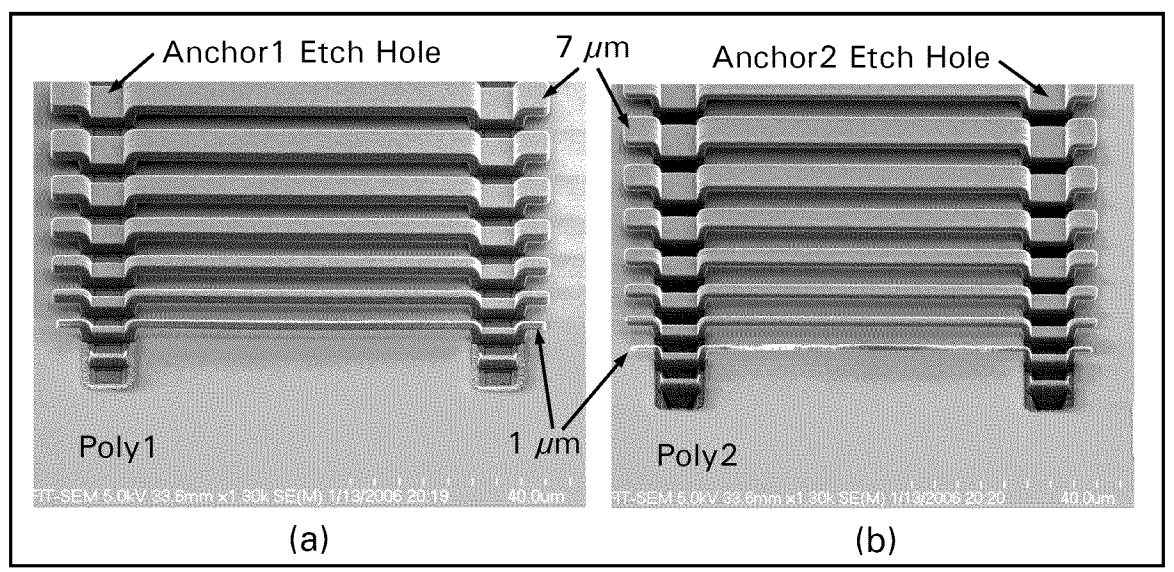


Figure 5-1. SEM images of width test structures showing that a minimum beam width of 1 μm survived the fabrication process for both (a) the Poly1 beam, and (b) the Poly2 beam. However, the Poly2 beam does not look to have very much structural rigidity.

Another process feature that is relevant to the design of the interrupter mechanism is the minimum spacing between similar layers. The minimum spacing is important because it ultimately determines the initial "closed" area of the interrupter aperture. For instance, the 2 µm separation selected for the interrupter plates designed in this thesis is what causes the 4-µm² open area when the interrupter aperture is closed, as discussed in section 4.5.1. If the minimum spacing could be reduced to 1 µm, the resulting "closed" area would decrease significantly to 1 µm². However, if the reduced spacing exceeded the capability of the fabrication process, the two interrupter plates could become permanently connected and would inhibit separation upon actuation. Figure 5-2 and Figure 5-3 shows the spacing test structures from both PolyMUMPs fabrication run #68 and #69, respectively. Clearly, the 2 µm spacing gap is successfully fabricated in both process runs. In addition, the 1 µm spacing gap, shown in Figure 5-3, should obviously be avoided.

A final fabrication process test that was performed as part of this research was the validation of the layer thickness data provided by MUMPs[®]. Since this thickness is known to vary for each fabrication, several measurements were taken of various structures fabricated in run #68 to see how they compare with the data provided by the MUMPs[®] foundry (see Appendix B). Furthermore, since the results of the actuator force tests are dependent on the actual thickness of the force measuring beams, precise layer thickness data is critical to producing accurate results. Additionally, the output force of the bent-beam actuator depends on the expanding thicknesses.

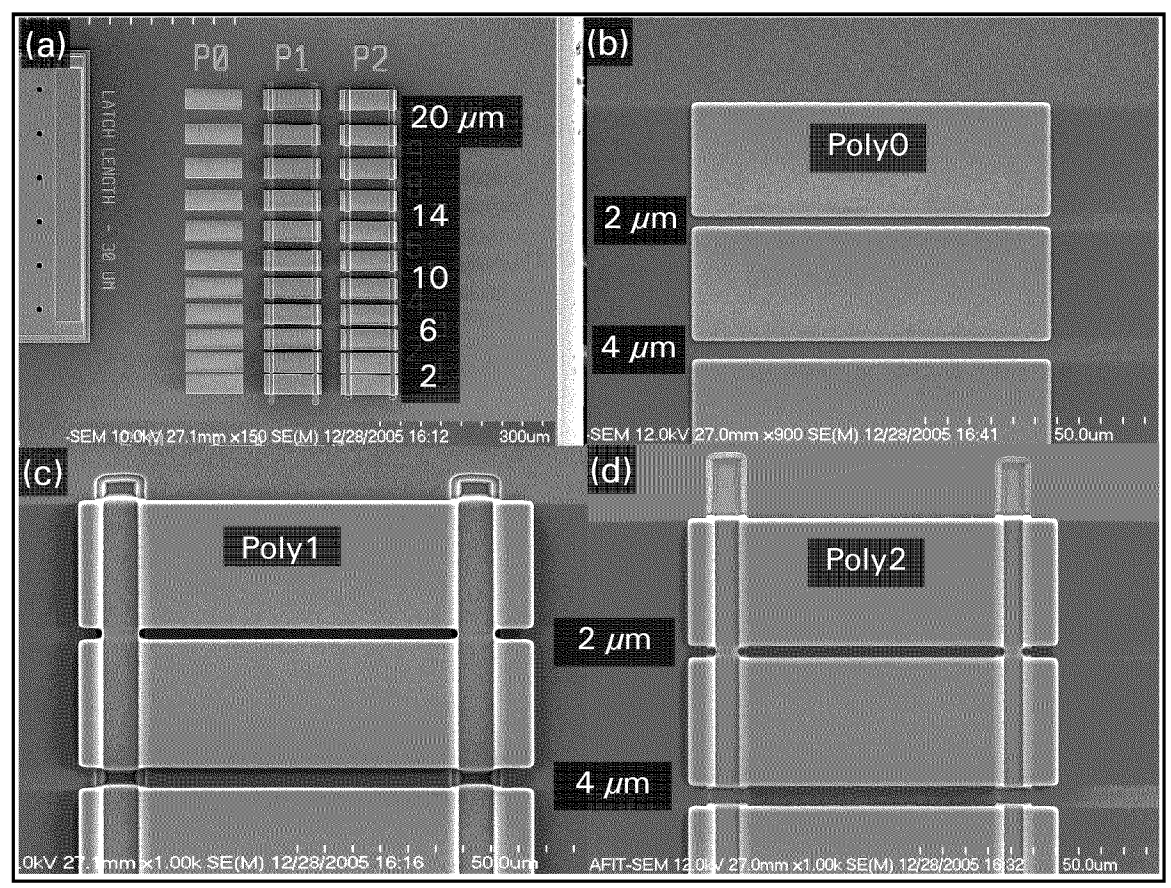


Figure 5-2. SEM images of the spacing test results for fabrication run #68: (a) Image of all three polysilicon layers with associated gap measurements, (b) Image of the Poly0 layer, (c) Image of the Poly1 layer, and (d) Image of the Poly2 layer. Note: the minimum spacing of 2 μ m could clearly be fabricated in this process run.

The optical profiler shown in Figure 4-5 was used to measure the vertical dimensions of the width test structures, the force measuring beams, and the expanding arms of the bent-beam actuator. To determine the thicknesses for each structure, approximately five to ten measurements were taken, then averaged to produce the measured thickness values shown in Table 5-1. An example of a measurement being taken with the optical profiler is shown in Figure 5-4. This example shows the spacing test structures being used to obtain a *single* measurement of the Poly0 thickness. All the other thickness measurements were taken in a similar manner.

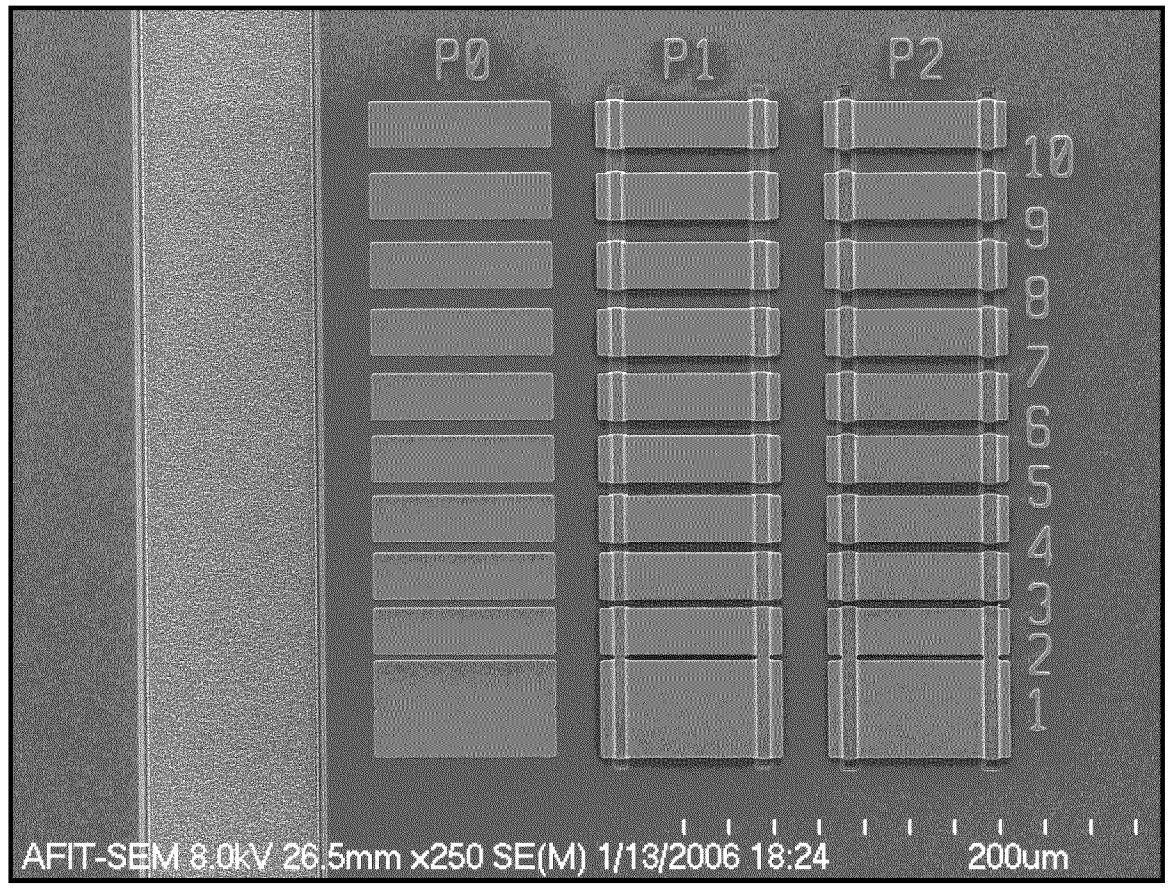


Figure 5-3. SEM image of the spacing test results for run #69 that includes the polysilicon layers – Poly0 (P0), Poly1 (P1), and Poly2 (P2). The numbers to the right represent the spacing between the two adjacent structures, in μm . Again, the 2 μm spacing is the minimum spacing gap that could be fabricated in this run. Clearly, the 1 μm spacing could not be fabricated in this process.

Table 5-1. Comparison between the average thicknesses measured for several fabricated structures and the thickness data provided by MUMPs[®] for run #68 [3].

	Poly0	Poly1 Beam (Ox1 + P1)* (μm)	Poly2 Beam (Ox1 + Ox2 + P2)* (μm)	Force Beam (Ox1 + P1 + P2)* (µm)	Actuator Arm $(Ox1 + P1 + P2)^*$ (μm)
	(μπ)	(μπ)	(μπ)	(1111)	(μπ)
Measured Thickness	0.5446	3.8275	3.7108	5.1124	5.1538
Std. Dev.	0.0021	0.0239	0.0162	0.033	0.0116
Run Data	0.4999	3.9732	4.1997	5.4337	5.4337
Percent Difference	8.55	3.73	12.36	6.09	5.29

^{*} Ox1 – Oxide1; Ox2 – Oxide2; P1 – Poly1; P2 – Poly2

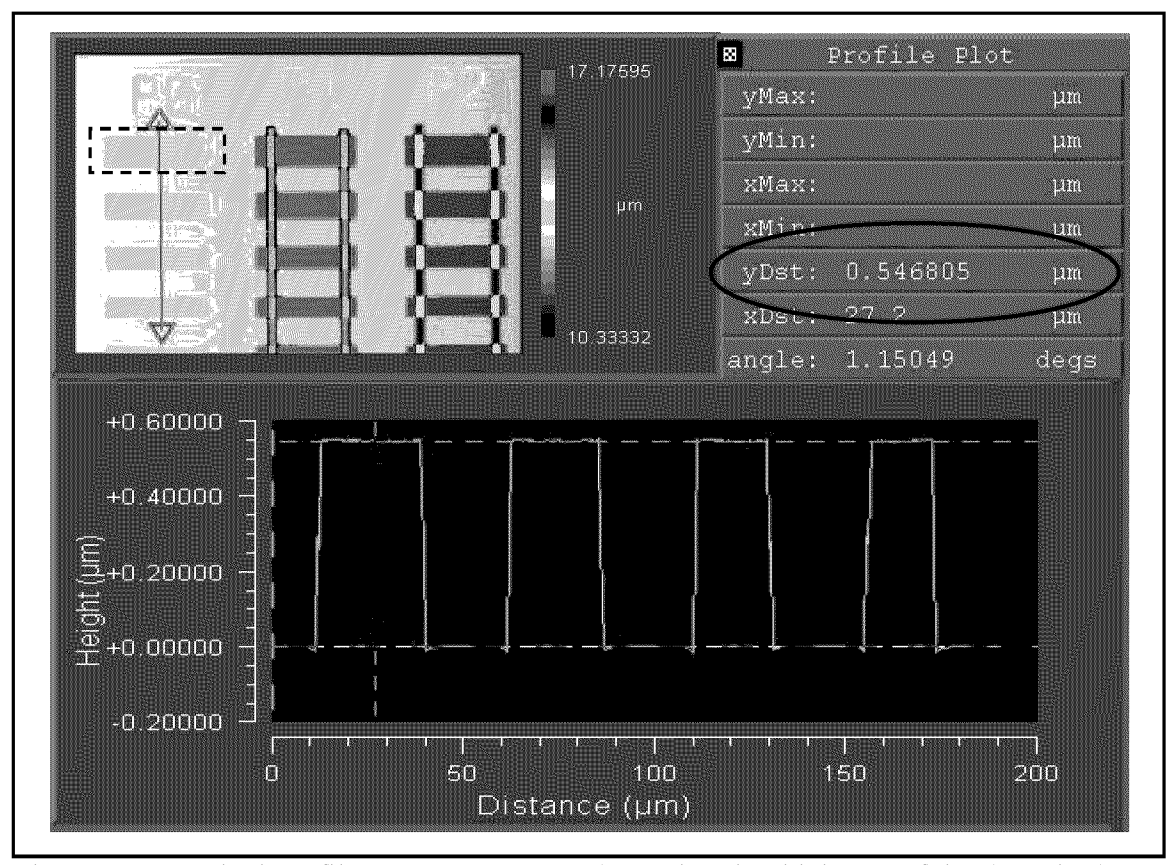


Figure 5-4. Optical profiler measurement to determine the thickness of the deposited polysilicon layer (Poly0). Note: the value shown is for only one measurement, and the reported values in Table 5-1 shows the average thickness values based on multiple measurements.

For the Poly1 and Poly2 fixed-fixed beams, measurements were taken at both the center and outer ends of the beams and the thickness values shown in Table 5-1 come from an average of both of these measurements. Differences between the vertical measurements taken from these two beam locations averaged 34 nm and 23 nm for both the Poly1 and Poly2, respectively. This is most likely due to the beam centers being slightly bowed up as a result of the compressive residual stress in both materials. In addition, since every structure, except Poly0, is a releasable structure, the thickness of the sacrificial oxide layer was accounted for in the run data values. The layer names that make up each releasable structure are also noted in Table 5-1.

The comparison between the measured thickness values and the values from the MUMPs® run data shows percent differences typically less than 10%. (The Poly2 beam was the only exception.) In addition, the measured values for the releasable layers are all slightly lower than the MUMPs® values. A possible cause for the lower measured values is that these structures are fabricated through a series of deposition and etch steps, which define the structure's final dimensions. Hence, the underlying materials tend to experience more etches than the higher layers, which causes them to be unexpectedly thinned [1]. This may also explain the relatively larger error in the Poly2 beam since it uses the most sacrificial layers (Oxide1 and Oxide2) in its fabrication. Because these measurements did not directly measure the individual Poly1 and Poly2 thicknesses, some uncertainty exists in the measured results. As a result, the thickness from the MUMPs® run data is used in Equation (4.7) to calculate the force of the bent-beam actuators.

5.2 Bent-Beam Electrothermal Actuator Experiments

In order to better understand the performance characteristics of the complete interrupter mechanism, a series of stand-alone bent-beam actuators were fabricated and tested to determine how they would perform on an individual basis. (The design layouts, for the specific actuators tested, are shown in Appendix C as Die #12 and Die #13.) The data gathered from these stand-alone tests should allow for a more complete analysis of the interrupter mechanism. For example, examining the input power required for each actuator to produce a given deflection can help determine which actuator is the most efficient. In addition, the output force of each actuator can be measured and compared with the power-deflection measurements to identify if one particular design is preferred over another. Recall, three different sets of bent-beam actuators were fabricated for the

interrupter mechanisms, and the design parameters chosen for each are summarized in Table 4-2.

5.2.1 Electrothermal Actuator Deflection Experiment

After performing the release procedures outlined in Appendix A, the individual bent-beam electrothermal actuators were tested on a Micromanipulator probe station. A specific set of actuators were designed to quantify the deflection characteristics of each type of actuator listed in Table 4-2. Moreover, a 400 μ m \times 12 *tapered* arm actuator configuration was also fabricated and tested, along with those listed in Table 4-2, in order to provide completeness. This additional actuator had the same design parameters as the Interrupter #2 actuator, except for the tapered arms. The electrical connection to the actuators was accomplished by placing two microprobes (tip radius of 0.5 μ m) on the gold probe pads incorporated into the anchors. Figure 5-5 shows one side of two 400 μ m \times 8 arm (straight and tapered) actuators prior to testing. This figure points out various elements that make up each actuator, such as the gold probe pads, the fabricated Poly0 scale used to measure deflection, and the tapered versus straight arm designs. The 400 μ m \times 12 arm actuators (not shown) are the same in every way except they have 12 arms instead of the eight shown in Figure 5-5.

To obtain the individual deflection characteristics for each actuator listed in Table 4-2, at least six identical actuators (from three different die) were tested. The only exception was for the 400 μ m \times 8 tapered arm actuator, where a total of nine identical actuators were tested. Hence, a total of 27 bent-beam electrothermal actuators were used to measure the deflection characteristics.

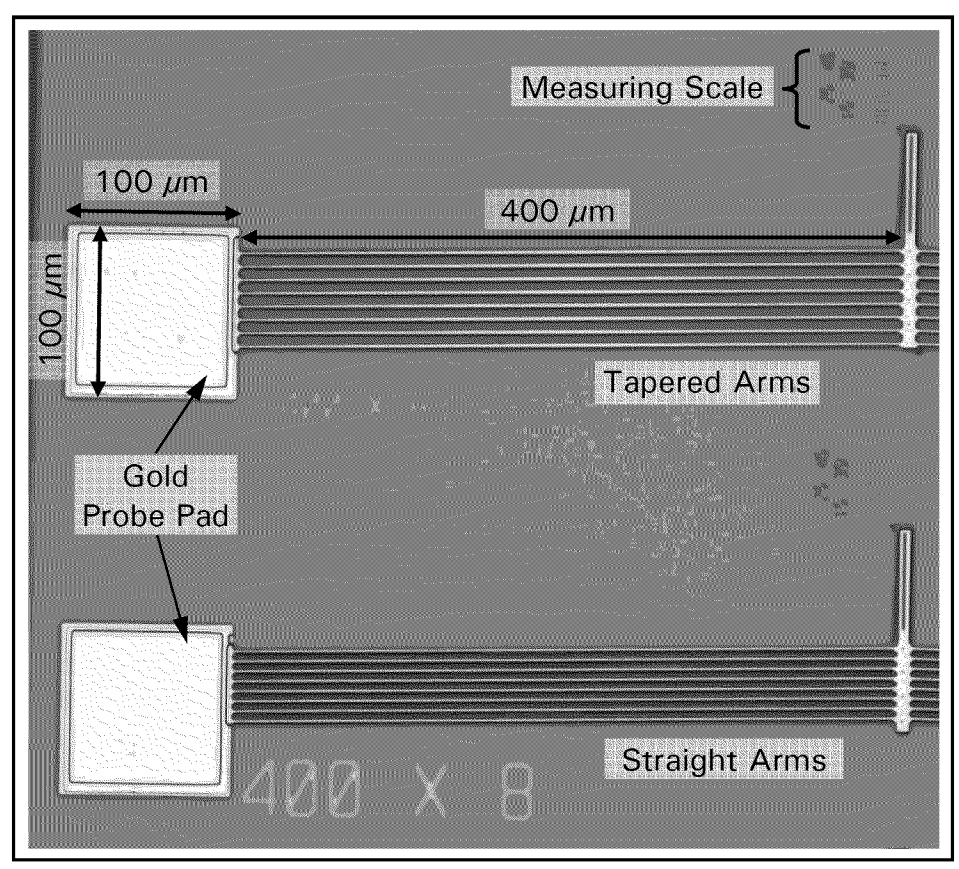


Figure 5-5. 20X magnification image of 400 μ m \times 8 arm (straight and tapered) electrothermal actuators. Note: the tapered arms are visibly thicker in the center of the arms than the straight arms.

To get a better understanding of the power requirements for the different actuators, the resistance of each actuator was measured and analyzed using an Agilent 34401A digital multimeter. Figure 5-6 shows the averaged resistance obtained from these measurements, with the error bars indicating one standard deviation. As shown, the actuators with 12 arms have a lower resistance than those with 8 arms.

To quantify this relationship, recognize that each expanding arm has a resistance given by [4]:

$$R = \frac{\rho \cdot l}{t \cdot w} \quad (\Omega) \tag{5.1}$$

where

 ρ = resistivity of polysilicon (Ω - μ m) l = total length of the arms (μ m) t = thickness of the arms (μ m) w = width of the arms (μ m)

Since each arm is designed to be the same length, thickness and width, they will all have the same resistance, R, as described by Equation (5.1).

Next, the entire actuator (neglecting the coupling beam) was modeled as a circuit consisting of parallel and series resistors that depend on the number of arm pairs, N, designed for the bent-beam actuator. The N-armed bent-beam actuator is shown in Figure 5-7(a). Subsequently, the actuator model can be reduced to a single resistive circuit with an equivalent resistance, R_a , as shown in Figure 5-7(b) and described by:

$$R_a = \frac{2 \cdot R}{N} \quad (\Omega) \tag{5.2}$$

where

N = number of arm pairs (Dimensionless)

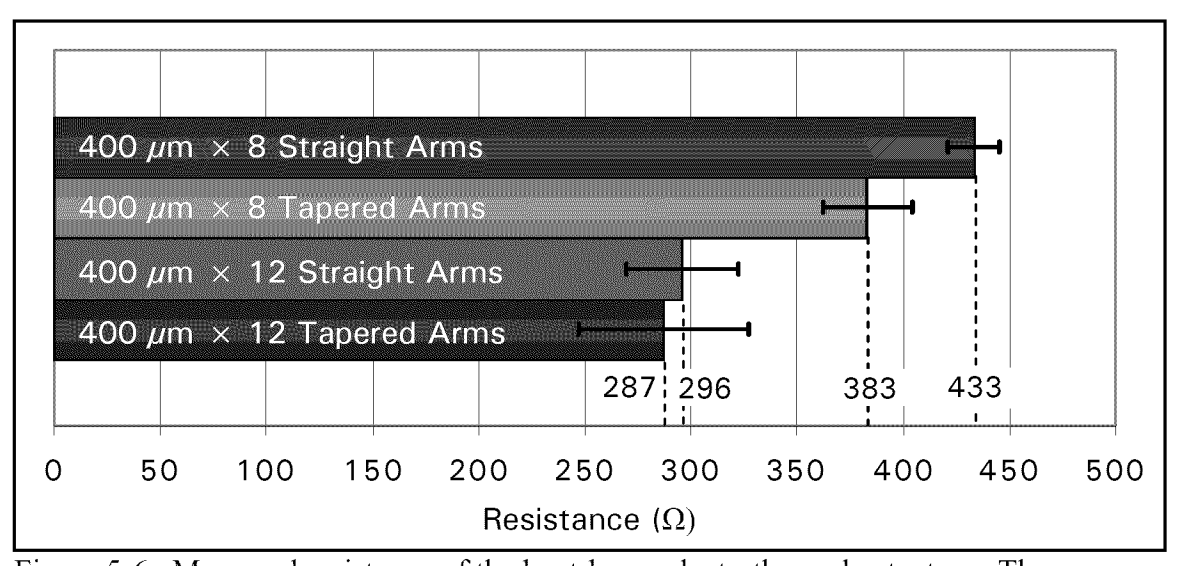


Figure 5-6. Measured resistance of the bent-beam electrothermal actuators. The error bars indicate one standard deviation from the mean.

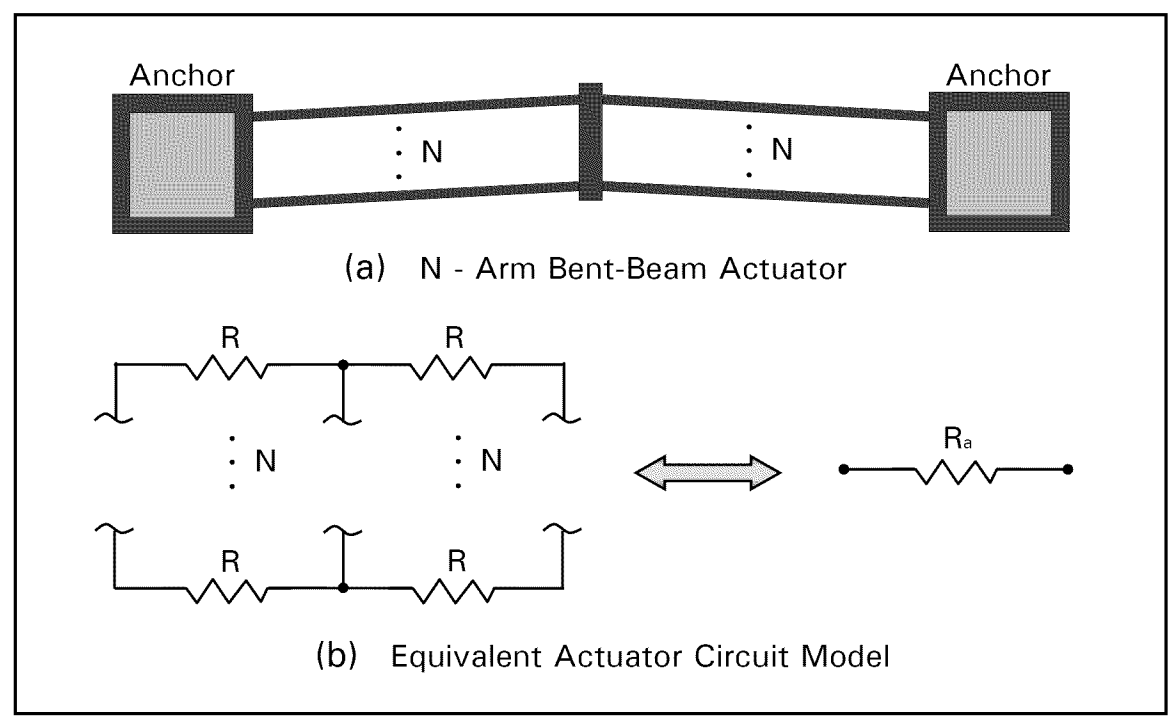


Figure 5-7. (a) Bent-beam electrothermal actuator with N arms. (b) Equivalent circuit model of the N-arm actuator showing its reduction into a single resistive element with an equivalent resistance, R_a , as described by Equation (5.2).

As a result of the relationship shown in Equation (5.2), an increase in the number of arms, N, will have the anticipated result of decreasing the resistance of the entire actuator, as was observed in Figure 5-6. Furthermore, it is expected that a decrease in resistance will cause a given deflection to require a larger input power, since more current will be needed to induce the same thermal expansion in the arms.

Figure 5-6 also shows that the actuators with tapered arms have a smaller resistance when compared to their counterparts with the same number of arm pairs. From Equation (5.2) this is also an expected result, since the resistance is inversely proportional to width. Without going into the details of width as a function of arm length, it can be intuitively appreciated that the width in the center of the tapered beams will be greater

than the width in the center of the straight beams, thus the resistance will decrease accordingly as shown in Figure 5-6.

To measure the deflection of the actuators as a function of input power, an Agilent 3631A DC power supply was used to step the input voltage from 0 V to 25 V (in one volt increments) and measure the current at each voltage step. Still images were captured for each voltage step using an Optronics DEI-750 microscope camera and ATI video capturing software. To determine the deflection of the actuator, the location of the actuator tip versus the fabricated Poly0 measuring scale was recorded (to an uncertainty of \pm 0.5 μ m) for each voltage step by observing the captured still images. This process was repeated for each of the 27 actuators and the data was tabulated and analyzed to produce the results shown in Figure 5-8 and Figure 5-9.

Figure 5-8 shows the measured deflection as a function of input power for the 400 µm × 8 tapered arm electrothermal actuator. The error bars indicate one standard deviation away from the average deflection at each particular voltage step. These results are based on measurements from nine different actuators that were fabricated on three different die. The intention of this figure is to show that repeatable results were obtained from this testing method. Thus, this testing method was repeated for each of the other 18 actuators, with similar precision being obtained.

Figure 5-9 shows the average deflection as a function of input power for all four bent-beam electrothermal actuators tested as part of this thesis. It can be seen that for a given input power, the 400 μ m \times 8 straight arm actuator produced the largest deflection. This is consistent with the tests performed by Szabo, which were summarized in Table 4-1. Moreover, the actuators with 8 arms also produced a greater deflection for a given

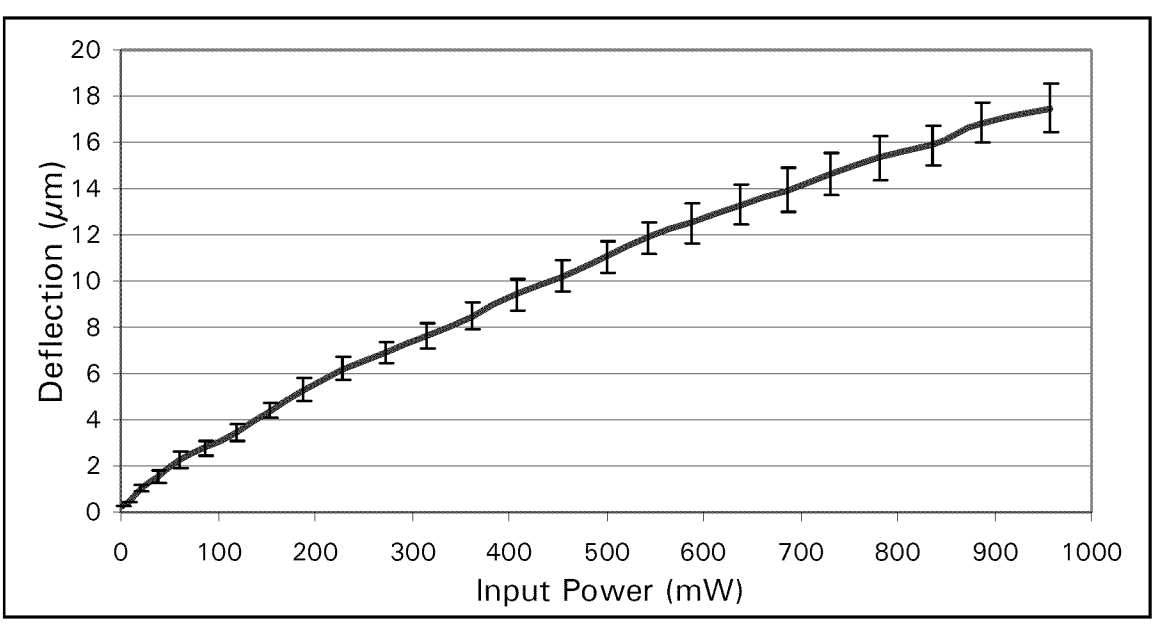


Figure 5-8. Average deflection as a function of input power for nine 400 μ m \times 8 tapered arm electrothermal actuators. The error bars indicate one standard deviation from the average deflection for each voltage step measured.

input power over those with 12 arms. Finally, when comparing the actuators with the same number of arms and input power, the actuators with tapered arms produced less deflection than those with straight arms. Therefore, it is easy to conclude that to produce the largest deflection with the smallest input power, a 400 μ m \times 8 straight arm actuator, would be preferred over a 400 μ m \times 8 tapered arm actuator, or a 400 μ m \times 12 arm actuator (either straight or tapered). Furthermore, a performance-to-energy analysis can be performed by comparing the deflection-to-power ratio at each voltage step for all four actuators. Figure 5-10 shows this comparison, and it is clear that the 400 μ m \times 8 straight arm actuator does indeed have advantages over the other actuators, if low power performance is required. In conclusion, the bent-beam actuators designed for the interrupter mechanism should be able to produce an aperture area of approximately 1300 μ m², based on Equation (4.8) and an actuator deflection of 17 μ m, as shown in Figure 5-9.

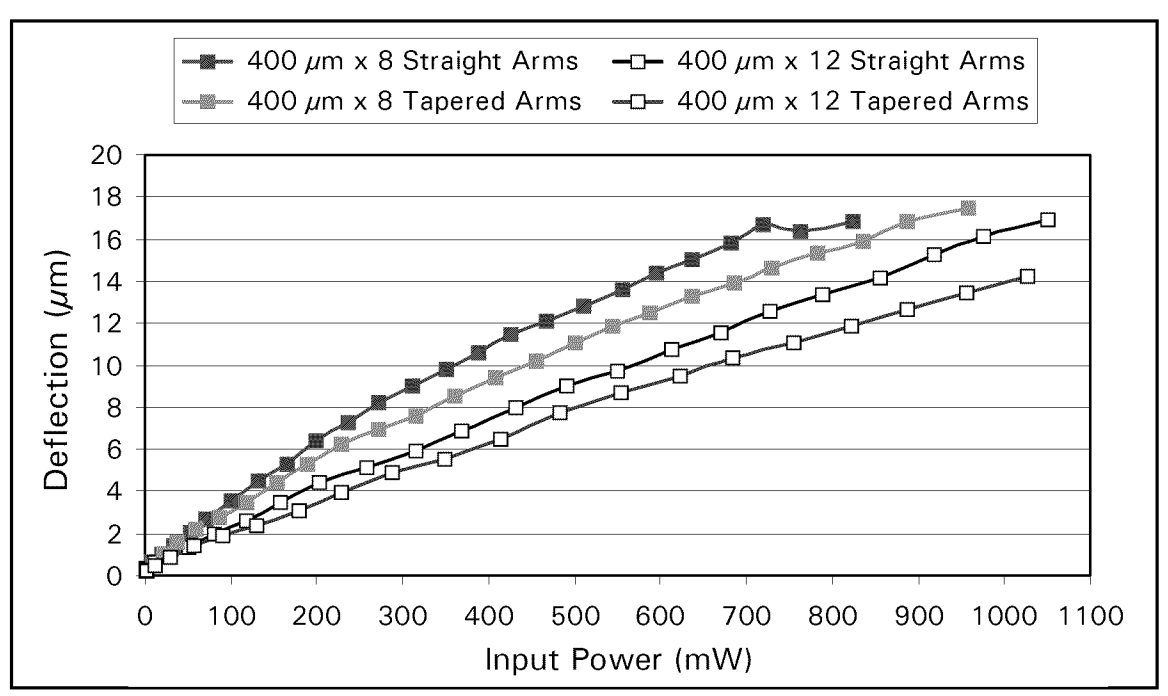


Figure 5-9. Average deflection as a function of input power for all four different bent-beam electrothermal actuators. For a given input power, the 400 μ m \times 8 straight arm actuator produced the largest deflection. Moreover, the actuators with 8 arms also produced a greater deflection for a given input power over those with 12 arms. Lastly, the tapered actuators produced less deflection than their straight armed counterparts.

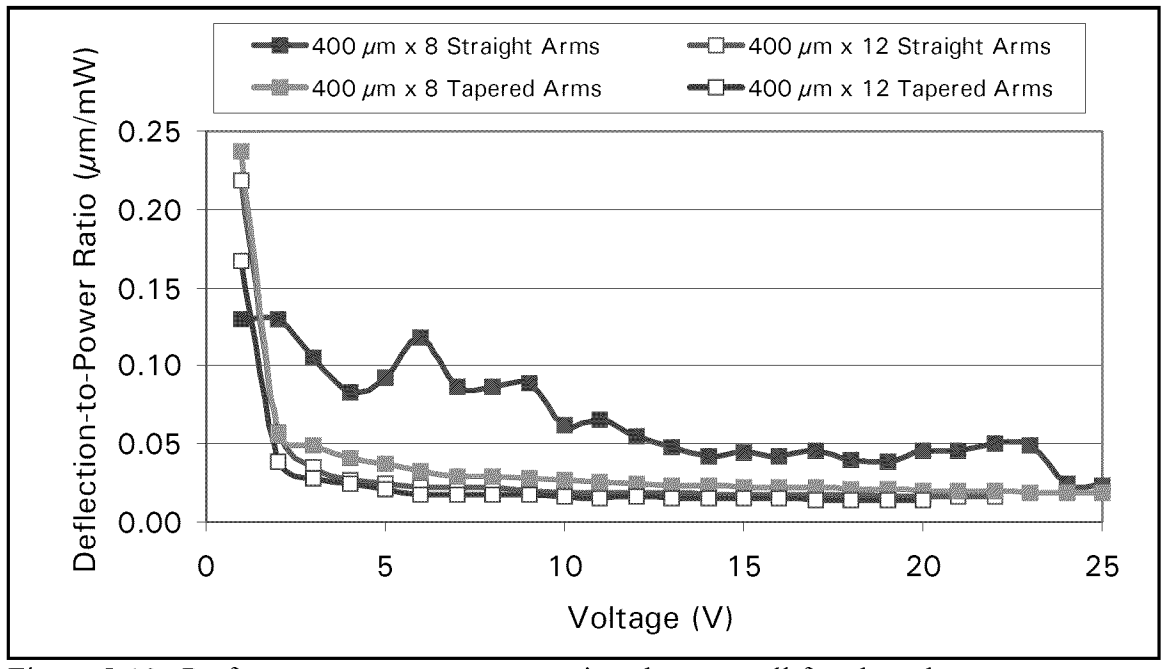


Figure 5-10. Performance-to-energy comparison between all four bent-beam electrothermal actuators. The deflection-to-power ratio at each voltage step is compared to show that the 400 μ m \times 8 straight arm actuator does indeed have advantages, over the other actuators, if low power performance is desired.

5.2.2 Electrothermal Actuator Force Experiment

In order to determine the output force for each type of bent-beam actuator, a set of three actuators (for each type) were fabricated adjacent to force measuring cantilever beams, as described in section 4.4.2. The cantilever beams for each set of actuators were designed for three different lengths: $100~\mu m$, $200~\mu m$, and $300~\mu m$. Figure 5-11 shows one set of actuators ($400~\mu m \times 8$ straight arms) with the three fabricated force measuring cantilever beams. In addition, for each cantilever beam length, three individual actuators of the same type (albeit from different die) were tested resulting in a total of nine actuators being tested for each type of actuator. Hence, a total of 36 bent-beam electrothermal actuators were tested to produce the force characteristics presented below.

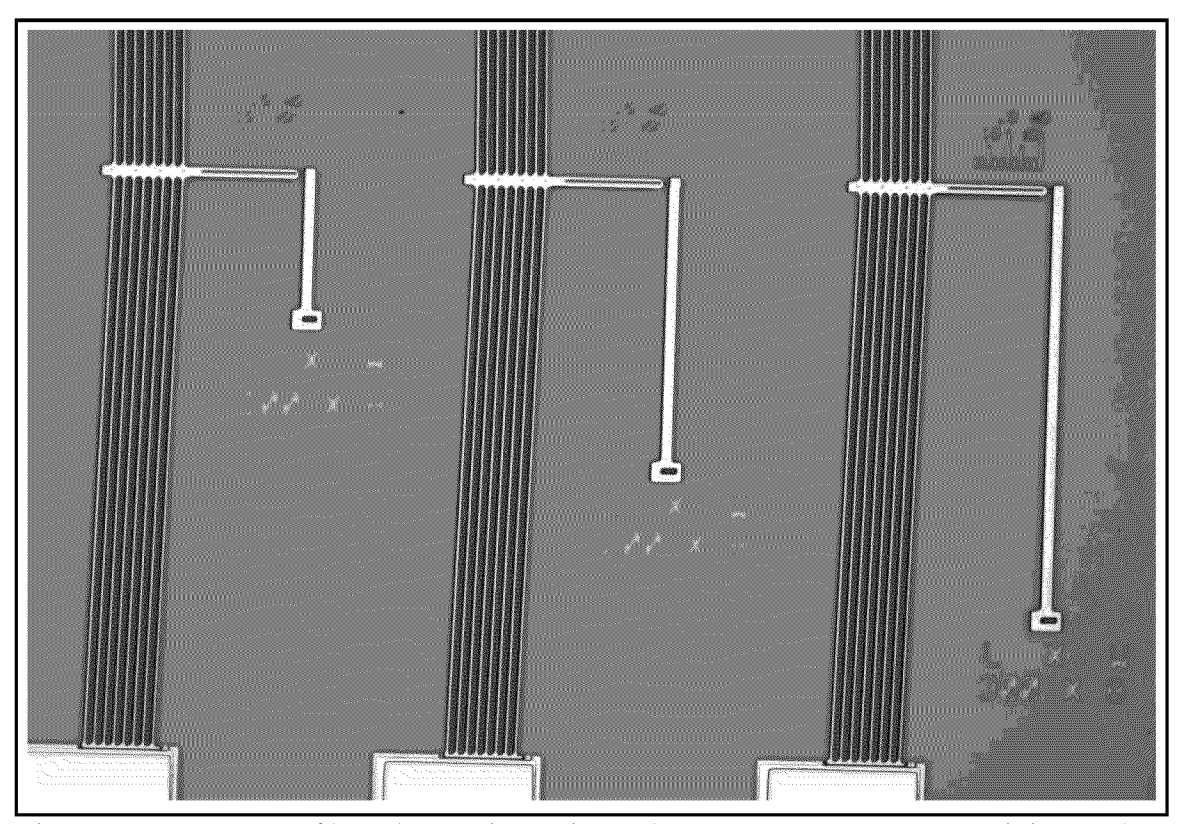


Figure 5-11. One set of bent-beam electrothermal actuators (400 μ m \times 8 straight arms) designed adjacent to the force measuring cantilever beams of three different lengths: 100 μ m, 200 μ m, and 300 μ m.

To measure the force as a function of input power, each actuator was placed on the Micromanipulator probe station and connected to the Agilent 3631A DC power supply in the same manner described in section 5.2.1. The actuator was driven by stepping an applied voltage from 0 V to 25 V, in one volt increments, while simultaneously measuring the current for each voltage step. In a similar manner to that described for the deflection measurements, still images of each voltage step were captured with the microscope's video equipment. Next, the maximum deflection was determined (to an uncertainty of \pm 0.5 μ m) by examining the still images and observing how far the cantilever beam moved before the actuator was no longer able to bend the beam. Figure 5-12 shows an example of the still images used to measure the maximum deflection data. This deflection value was recorded three times for each actuator type, and each cantilever beam length, until the entire batch of 36 force measuring actuators were tested.

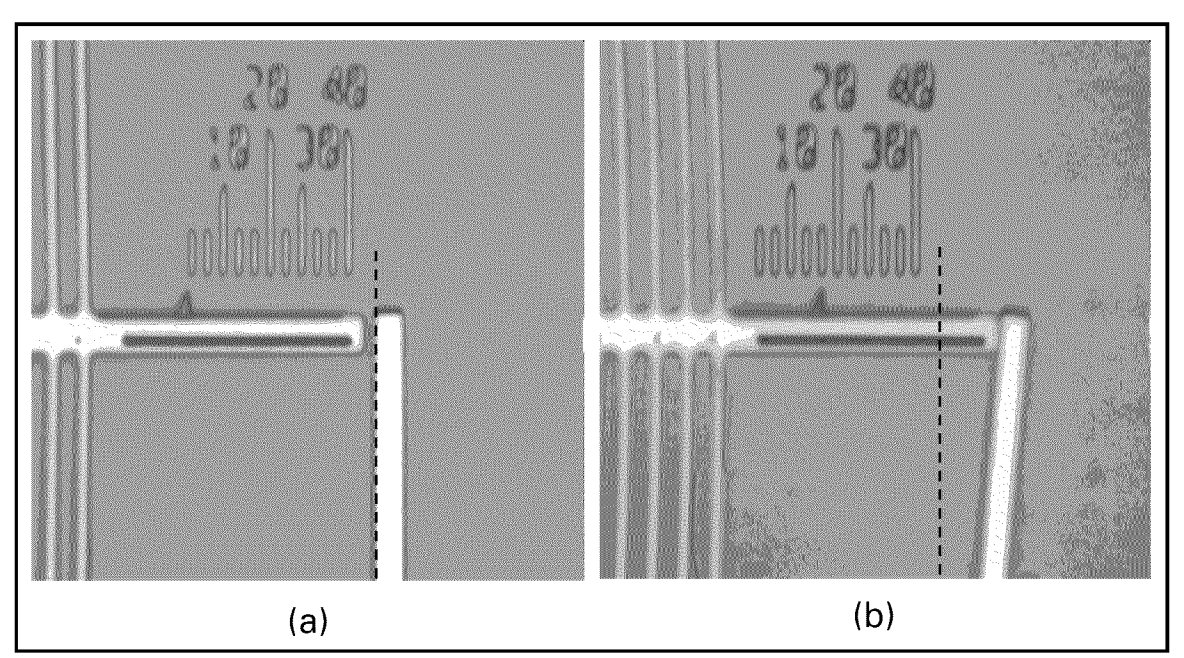


Figure 5-12. (a) Image of the 400 μ m \times 8 tapered arm actuator at 0 V. (b) Image of the same actuator at 23 V and a maximum cantilever beam deflection of 11 μ m. Note: the dashed lines represent the initial beam location.

It is important to note that the maximum deflection of the cantilever beam is not the maximum deflection of the actuator, because the actuator and cantilever beam are initially separated by a 2.5 μ m gap. This gap is intended to satisfy the design rules to ensure the two separate structures are not inadvertently fabricated as one structure. Figure 5-13 shows an SEM image of a 400 μ m \times 8 straight arm actuator with a 100 μ m cantilever beam. The inset shows a magnified view of the 2.5 μ m gap.

Equation (4.7) is used to calculate the output force, yet a few other cantilever beam parameters (thickness, width, and length) must be known. The thickness of the

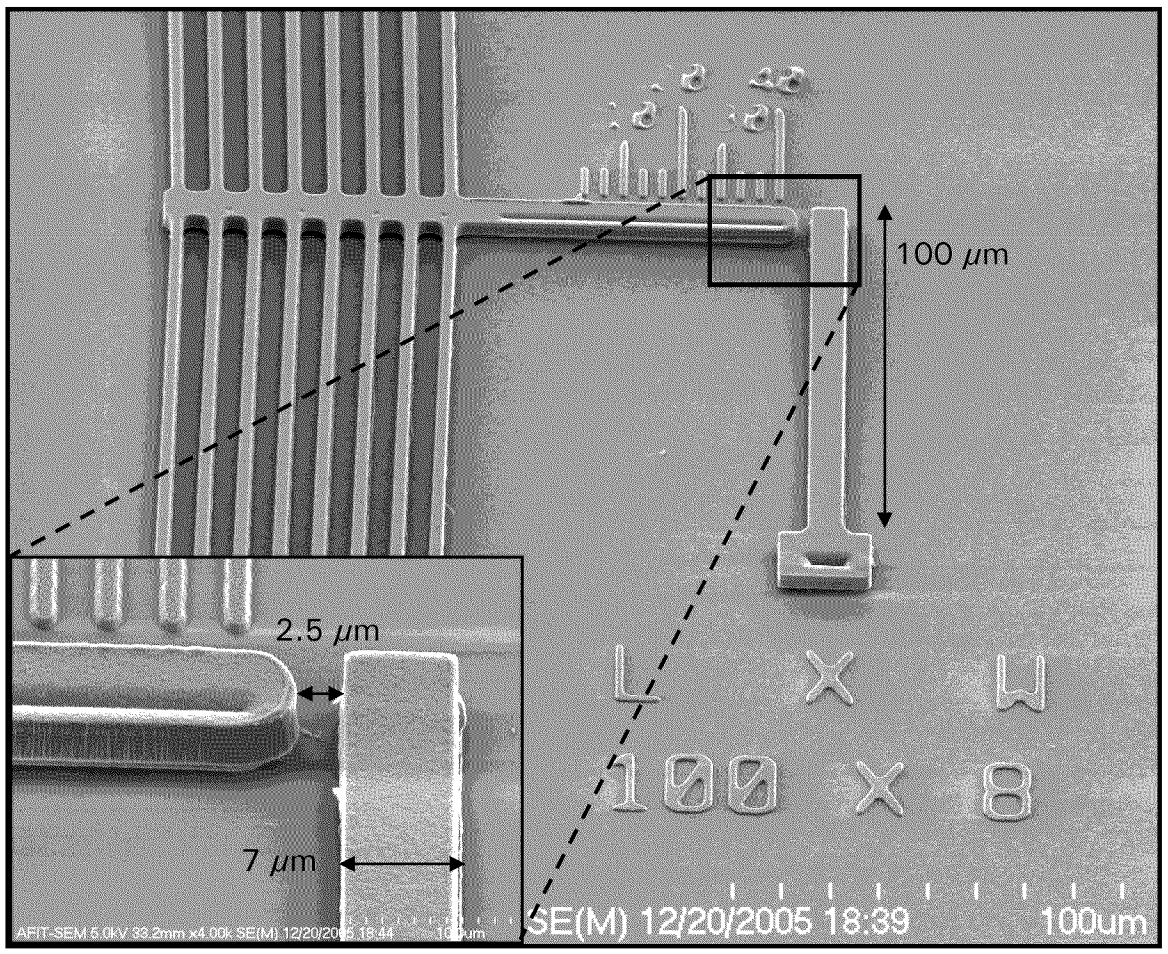


Figure 5-13. SEM image of a 400 μ m \times 8 straight arm actuator with a 100 μ m force measuring cantilever beam. The inset shows the 2.5 μ m gap that must be accounted for in determining the maximum deflection of the cantilever beam, along with the measured width of the beam.

beam is taken from the PolyMUMPs run data provided in Appendix B, which is 3.4527 μ m for the stacked (Poly1 + Poly2) beam. The width of the beam was designed to be 8 μ m; however measurements taken in the SEM indicated that the fabricated width is 7 μ m \pm 0.25 μ m. The lengths of the beams were designed to be either 100 μ m, 200 μ m, or 300 μ m, and since multiple measurements of these lengths produced very little deviation from the exact designed lengths, no adjustments were made to the designed values. Finally, a Young's modulus of 158 GPa [5] was used for the polysilicon cantilever beam.

The maximum beam deflection, d_{max} , used in calculating the output force, comes from the average (measured) maximum deflection produced by each actuator type, for each cantilever beam length. Consequently, three different measurements are used to evaluate the value for the average maximum beam deflection. Table 5-2 summarizes the results of the force measuring tests, to include, the average maximum deflection used to calculate the output force in Equation (4.7), the standard deviation produced by these three measured values, and finally, the calculated output force for each actuator type.

For every actuator type (except the 400 $\mu m \times 8$ straight arm actuator) the calculated output force is reasonably consistent whenever either the 100 μm or 200 μm cantilever beams are used to determine the maximum deflection values. In contrast, the 300 μm beam consistently results in a significantly lower output force for all actuator types (by approximately 50%) when compared to the other two cantilever beam lengths. The most likely cause for this is that the maximum deflection of the 300 μm beam exceeds the maximum deflection capability of the actuator. By examining the graph of Equation (4.7) shown in Figure 4-17, and assuming the other calculated output forces are correct, it can be seen that the maximum deflection for the 300 μm beam occurs at

approximately 19 μ m for the 8 armed actuators and approximately 24 μ m for those with 12 arms. Clearly, none of the actuator types were capable of deflecting 24 μ m, and 19 μ m was just above the deflection limit for the unloaded actuators, as shown in Figure 5-9. As a result, the force produced by the 300 μ m beam was considered to be invalid, and only the results from the 100 μ m and 200 μ m cantilever beams were considered valid.

Table 5-2. Summary of the data collected from the bent-beam actuator force measurement tests to include, the average maximum beam deflection (based on three actuators of each type), the standard deviation, and the calculated output force. Note: the calculated force for the 300 μ m beam is considered invalid because the required maximum beam deflection exceeds the maximum deflection capability of the actuator.

Actuator Type		Cantilever Beam Length (µm)		
Actuator Type		100	200	300
400 μm × 8 Arm [Straight]	Ave. Max. Beam Deflection (µm) (Std Dev)	0.67 (0.14)	11.00 (2.65)	13.17 (1.15)
	Calculated Force (µN)	31.19	64.32	22.81
400 μm × 8 Arm [Tapered]	Ave. Max. Beam Deflection (µm) (Std Dev)	1.00 (0.00)	8.33 (2.31)	15.0 (1.73)
	Calculated Force (µN)	46.78	48.73	25.99
400 μm × 12 Arm [Straight]	Ave. Max. Beam Deflection (µm) (Std Dev)	1.25 (0.25)	10.75 (1.06)	12.50 (0.50)
	Calculated Force (µN)	58.47	62.86	21.66
400 μm × 12 Arm [Tapered]	Ave. Max. Beam Deflection (µm) (Std Dev)	1.42 (0.14)	10.33 (4.16)	15.83 (0.29)
	Calculated Force (μN)	66.27	60.42	27.43